Evaluation of the Effect of Sulfur on the Performance of Nickel/Gadolinium-Doped Ceria Based Solid Oxide Fuel Cell Anodes

Matthias Riegraf,* Vitaliy Yurkiv, Rémi Costa, Günter Schiller, and K. Andreas Friedrich[a]

The focus of this study is the measurement and understanding of the sulfur poisoning phenomena of Ni/gadolinium-doped ceria (CGO) based solid oxide fuel cells (SOFC). Cells with Ni/CGO10 and NiCu5/CGO40 anodes were characterized by using impedance spectroscopy at different temperatures and H_2/H_2O fuel ratios. The short-term sulfur poisoning behavior was investigated systematically at temperatures of 800–950 °C, current densities of 0–0.75 A cm^{-2}, and H_2S concentrations of 1–20 ppm. A sulfur poisoning mitigation effect was observed at high current loads and temperatures. The poisoning behavior was reversible for short exposure times. It was observed that the sulfur-affected processes exhibited significantly different relaxation times that depend on the Gd content in the CGO phase. Moreover, it was demonstrated that the capacitance of Ni/CGO10 anodes is strongly dependent on the temperature and gas-phase composition, which reflects a changing Ce^{3+}/Ce^{4+} ratio.

Introduction

Over the last few decades, the challenges associated with global warming and the progressing depletion of natural resources have sparked increasing interest in the development of highly efficient electrochemical energy devices that allow the use of a variety of renewable fuels such as hydrogen, syngas, and biogas. In this context, as a result of their high operating temperatures that give rise to fast electrode reaction kinetics, solid oxide fuel cells (SOFC) are a promising technology as they are able to convert hydrocarbons, CO, and biofuels readily without the necessity to employ noble metals as catalysts.[1] However, both biogas and natural gas usually contain undesirable sulfur-containing species that lead to the poisoning of Ni-containing fuel electrodes, which leads to a significant SOFC performance decrease within a short time. The sulfur poisoning of the commonly used Ni/yttria-stabilized zirconia (YSZ) cermet anodes has been investigated widely, both experimentally and theoretically.[2–7] However, in comparison to Ni/YSZ, fewer studies on the sulfur poisoning behavior of Ni/CGO anodes exist, although they show a significantly higher sulfur tolerance than Ni/YSZ.[8–15] Thus, the underlying microscopic processes that define the performance characteristics and the sulfur poisoning behavior of Ni/CGO electrodes are not yet fully understood.

Recent studies on the electrochemical reactivity of Ni/CGO anodes have observed fundamental differences to Ni/YSZ in the fuel oxidation mechanisms.[16–18] Hence, to explain the high sulfur resistance of Ni/CGO, an advanced understanding of the fuel oxidation mechanism is required. The present state of knowledge is reviewed briefly in the following section.

Fuel oxidation mechanism on Ni/doped ceria anodes

Although the drastic performance decrease of SOFC with Ni/YSZ anodes was shown to be related to Ni surface poisoning with elemental sulfur, recent fundamental studies of Ni/CGO anodes have observed that the electrochemistry takes place on the CGO rather than on the Ni surface. Thus Ni was suggested to act primarily as an electronic conductor.[16–18] Under common SOFC operating conditions (temperatures above 700 °C and a reducing atmosphere), CGO displays high surface activity towards H_2 and CH_4 oxidation and mixed ionic and electronic transport properties because of the mixed oxidation state of Ce, which can hop easily between Ce^{3+} and Ce^{4+}. This phenomenon could extend the electrochemical reaction zone in the composite electrodes from the triple phase boundary (TPB) to the double phase boundary (2PB) interface between ceramics and gas.[8,13,16,17,19–23] Thus, the spillover of reaction intermediates at the TPB between the ceramic and metallic phase that occurs in Ni/YSZ anodes is likely not the rate-limiting step during hydrogen oxidation on Ni/CGO.[16,17,21–23]

Recently, it was suggested that hydrogen oxidation proceeds via an OH$^-$ intermediate that binds to the surface vacancies.[19] The adsorption of hydrogen and water on the surface oxygen vacancies was observed experimentally to be very fast and

[a] M. Riegraf, Dr. V. Yurkiv, Dr. R. Costa, Dr. G. Schiller, Prof. Dr. K. A. Friedrich
Institute of Engineering Thermodynamics
German Aerospace Center (DLR)
Pfaffenwaldring 38–40, 70569 Stuttgart (Germany)
E-mail: matthias.riegraf@dlr.de

hence, can be assumed to be quasiequilibrated. In this context, the electron transfer between the OH^- intermediate and Ce^{4+} was suggested to be the rate-determining step in the hydrogen oxidation process. Impedance spectroscopy on symmetrical cells was used in several studies in which two distinct contributions in the spectra of Ni/CGO anodes were described, both of which are ascribed to actual electrode processes.[22, 24–27] The capacitive nature of at least one of these processes was related to a surface double layer. Such capacitance is observed frequently in mixed ionic electronic conductor (MIEC) electrodes and is caused by the accumulation of electronic charges in the space-charge layer of the MIEC surface and adsorbed ions on the surface.[28–30]

Although the process at middle frequencies (20–100 Hz) was interpreted recently to represent the electrochemical oxidation of hydrogen that includes charge transfer,[22, 27, 31] other studies assigned this impedance feature to oxide ion transport in the MIEC itself or across the electrolyte–MIEC interface.[22, 24] With regard to the process at lower frequencies (0.1–10 Hz), no definite assignment has been achieved so far. This process has been shown to be dependent on the active surface area of the doped ceria phase and was, therefore, assigned to a surface process. Hydrogen adsorption coupled to surface diffusion on CGO was suggested as well.[21, 24, 25] In the described studies, electrodes with different Gd-doping contents between 10–40% are employed. The different interpretations of the observed impedance processes give rise to the assumption that different Gd-doping levels could lead to fundamental differences in the cell Behavior.

Sulfur poisoning of Ni/CGO anodes

Several research groups have investigated the influence of sulfur-containing fuels on Ni/CGO-based SOFC performance experimentally.[8–15] However, there is a significant discrepancy between these studies with regard to the interpretation of the results. In most cases, a rapid initial power output drop occurs for H_2S concentrations in the ppm level with an accompanying increase in total anode resistance. Upon poisoning with 2 ppm H_2S, Kavurucu Schubert et al. observed a power output drop of less than 2% and a full recovery after switching off the H_2S supply.[8] Moreover, Aravind et al. did not witness any effect on the impedance spectra after sulfur poisoning with 9 ppm H_2S.[11] In studies that investigated the influence of higher H_2S concentrations, the formation of Ce_2O_2S was observed.[32] However, ceria and Ni were shown not to form any bulk sulfide phases at H_2S concentrations higher than 100 ppm.[33] A few studies compared the sulfur poisoning of Ni/CGO and Ni/YSZ anodes directly, and the poisoning behavior was observed to be remarkably similar as the saturation of the resistance increase levels off with the increasing H_2S concentration in the same manner for both anodes. Consequently, the sulfur poisoning of Ni/CGO anodes has been interpreted frequently under the assumption that the underlying mechanism is the same as that for Ni/YSZ and, therefore, has not yet been subject to the same detailed analysis. Although the performance drop upon the sulfur exposure of SOFC with Ni/YSZ anodes

was related to the sulfur surface blockage of Ni, this is unlikely to have an influence on Ni/CGO anodes if Ni acts as a pure electronic conductor, which leaves the real impact of sulfur unclear. Recently, it has been reported that pure CGO anodes without a metallic phase also suffer from sulfur poisoning under exposure to 10 ppm H_2S, which demonstrates the possibility of sulfur adsorption on the ceramic and the corresponding active surface blockage.[34] The possible sulfur poisoning of ceria surfaces at high temperatures was further demonstrated by Mullins and McDonald by using temperature-programmed desorption (TPD) experiments combined with soft X-ray photoelectron spectroscopy (sXPS). The authors investigated the H_2S exposure of reduced $CeO_2(111)$ surfaces and showed that hydrogen sulfide dissociates on the surface vacancies to OH and SH and further into elemental sulfur.[35] They showed that either H_2 or H_2O desorb at approximately 600 K, whereas sulfur remains on the oxygen surface vacancy sites at higher temperatures. However, the authors indicated that above 800 K sulfur could diffuse into the bulk phase of ceria. Besides that, they could not detect any SO_x products in the exhaust gas.[35]

To shed more light on the sulfur poisoning process of Ni/CGO anodes, in the present work the impact of hydrogen sulfide on Ni/CGO10 and Ni/CGO40-based anodes is investigated systematically with a variation of the temperature, current density, and H_2S concentration. Subsequently, this impact is evaluated by taking into account findings published recently to give an insight into the corresponding fuel oxidation mechanism.

Results and Discussion

The main objective of the present study is to establish the influence of sulfur poisoning on Ni/CGO-based anodes. Therefore, two kinds of Ni/CGO anodes with different Gd-doping levels were studied. However, before the detailed investigation of the poisoning phenomena, a fundamental understanding of the fuel oxidation mechanism on CGO-based anodes is necessary. For this reason, the general approach is to compare different electrochemical measurements by employing two types of anodes (cell A and cell B) towards electrocatalytic reactivity with and without sulfur-containing fuels. Firstly, we present the extensive characterization of the cells in non-sulfur systems and, subsequently, the sulfur poisoning behavior of the investigated cells.

Identification of physicochemical processes in non-sulfur systems

Ni-CGO10-based cell

The current density–voltage (i–V) curves of cell A in a H_2/H_2O (97:3) mixture and with the stepwise variation of the temperature from 650 to 950 °C are shown in Figure S2. The current density at 0.7 V reaches 0.93 A cm^{-2} at 850 °C, which demonstrates the high performance of the cell. The Nyquist plot of the impedance spectra measured at different operating temperatures is shown in Figure 1a, and the corresponding imaginary impedance plot is shown in Figure 1b. Analogously, the
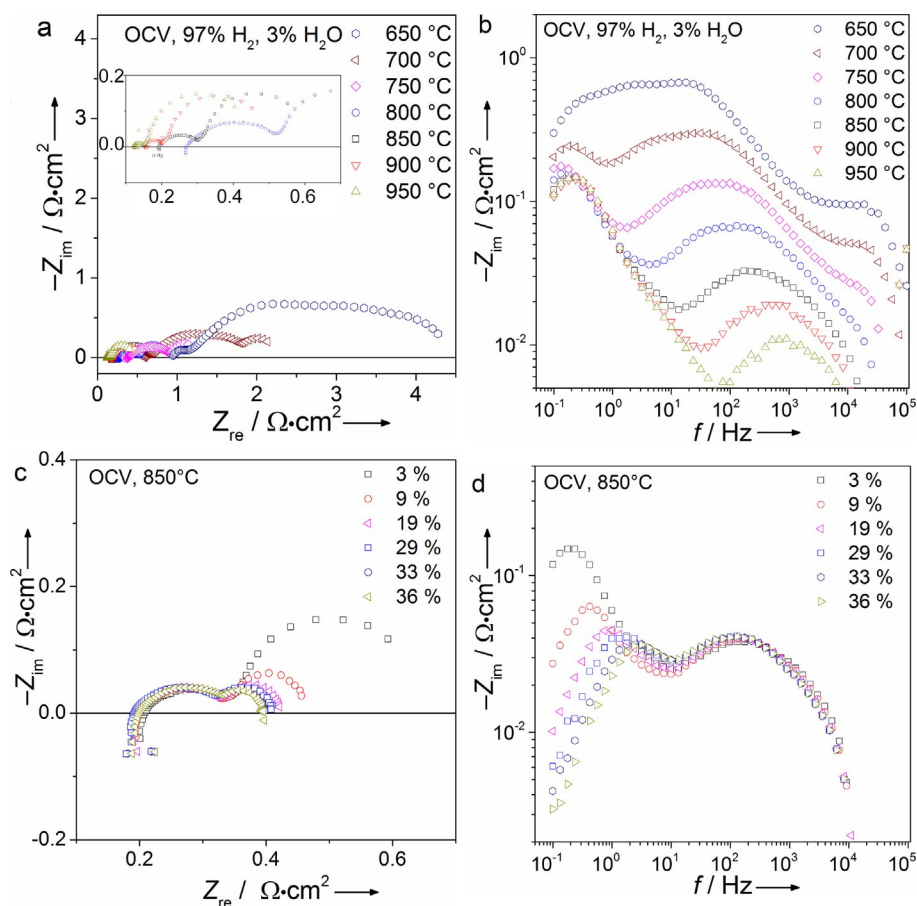
Figure 1. a) Nyquist and b) imaginary impedance plot of the impedance spectra of Ni/CGO10-based SOFC measured at $T = 650–950\,°C$, OCV, $pO_2 = 0.21$ atm, $pH_2 = 0.97$ atm, and $pH_2O = 0.03$ atm, c) Nyquist and d) imaginary impedance plot of impedance spectra measured at $T = 850\,°C$, OCV, $pO_2 = 0.21$ atm, and $pH_2O = 0.03–0.36$ atm.

Nyquist and imaginary impedance plots of data recorded at different humidity levels at 850 °C are presented in Figure 1 c and d. Clearly, the Nyquist plots at higher temperatures show two separated arcs, which is also observed commonly for SOFC with Ni/YSZ anodes. The peak frequency of the middle-frequency arc lies at approximately 200 Hz at 850 °C, whereas the low-frequency peak is at approximately 0.2 Hz (Figure 1 b). With decreasing temperature, the middle-frequency contribution can be further distinguished into two peaks. For example, at 700 °C, one contribution is visible at approximately 35 Hz and the other is at 5 Hz. Both contributions show thermal activation and, thus, can be interpreted as physicochemical electrode processes.

A temperature dependence in the low-frequency region is also observed in the data shown in Figure 1 a and b, which indicates the existence of a thermally activated electrode process in addition to a gas conversion process that is expected to have only a small temperature dependence.[36,37] The peak frequency of the low-frequency contribution shifts to higher frequency values between 750 and 650 °C. This is unusual for thermally activated processes, which usually exhibit a peak shift to lower frequencies caused by an increase in resistance under these conditions. Consequently, the observed behavior must be caused by a significant decrease of capacitance with

decreasing temperature, according to the relationship $f_S = 1/(2\pi RC)$ in which R is the process resistance, f_S is the peak frequency, and C is the capacitance. This change in capacitance will also be further discussed in the following sections. At temperatures higher than 800 °C, the peak frequency and peak intensity stay constant, which indicates a less temperature-dependent behavior of the low-frequency arc in this region. This could suggest that at higher temperatures, the gas conversion dominates the low-frequency arc, whereas at lower temperatures the physicochemical anode process prevails. In the present study, thin anodes ($< 30\,\mu m$) are employed, therefore, resistances caused by porous transport are negligible.[38]

An increase of pH_2O leads primarily to a strong reduction of the low-frequency contribution in the impedance spectra at a frequency range of 0.1–1 Hz (Figures 1 c and d). Although this is expected for gas conversion, the strong reduction of the peak also suggests an enhancing effect of the increasing water partial pressures on the kinetics of the low-frequency process. This suggests that the origin is an anode surface process as already observed in symmetrical cell measurements of Ni/CGO10 anodes at similar frequencies.[26,27,39] The middle-frequency contribution of the impedance spectra at frequencies greater than 100 Hz is not affected by pH_2O, which indicates the absence of a surface anode process in this region.

The replacement of the air supply with pure oxygen at 850 °C leads to a reduction of the middle-frequency peak mainly in a frequency range of approximately 50–100 Hz (Figure S3). This confirms the existence of a cathode surface process in this region, which is also in accordance with previous studies of lanthanum strontium manganite (LSM)/YSZ cathodes.[40–42] However, the reduction of the cathode contribution in the impedance spectra still leaves a significant middle peak contribution in the impedance spectra at a frequency of approximately 200 Hz, which indicates the existence of another anode process in this region. This is consistent with previous studies on symmetrical Ni/CGO cells that show one middle- and one low-frequency contribution.[24,27] Although these studies report the low-frequency contribution to be dependent on the anode gas-phase composition, the middle-frequency process was not affected, which led to its attribution to an anode bulk process. The origin of this middle-frequency bulk process was suggested to be oxide ion transport from the bulk to the surface or across the electrolyte–anode interface.[24,25] The low-frequency contribution is not caused by gas diffusion as the corresponding process was reported to be thermally activated.[24,27] Primdahl and Liu attributed this process to hydrogen adsorption and dissociation, possibly connected with a surface diffusion process as they observed a considerable resistance decrease upon the addition of a small catalytic amount

(0.8 wt %) of Ni.[25] Moreover, the process showed an isotope mass effect, which would be expected from hydrogen adsorption and dissociation.[24]

In summary, two processes could be identified in the impedance spectra of cell A. One middle-frequency process is not affected by humidity, therefore, it is ascribed to a bulk process. Additionally, one low-frequency process was shown to be pH$_2$O dependent, hence it is attributed to a surface process.

Ni/CGO40-based cell

The i–V curves of cell B are presented in Figure S4. The current density at 0.7 V reaches more than 0.5 A cm^{-2} at 800 °C and thus the performance of cell B is slightly lower than that of cell A (0.62 A cm^{-2} at 800 °C). The Nyquist plot of the impedance spectra measured at different operating temperatures of 700–950 °C is shown in Figure 2 a, and the corresponding imaginary impedance representation is shown in Figure 2 b. Analogously, Nyquist and imaginary impedance plots for different pH$_2$O at 850 °C are shown in Figure 2 c and d. In the Nyquist plots, two clearly separated arcs can be distinguished. The peak frequencies of the high-frequency arc lie between 10^1 and 10^2 Hz at common electrolyte-supported cell (ESC) operating temperatures above 800 °C (Figure 2 b). Notably, there is also a cathode process present at frequencies of approxi-
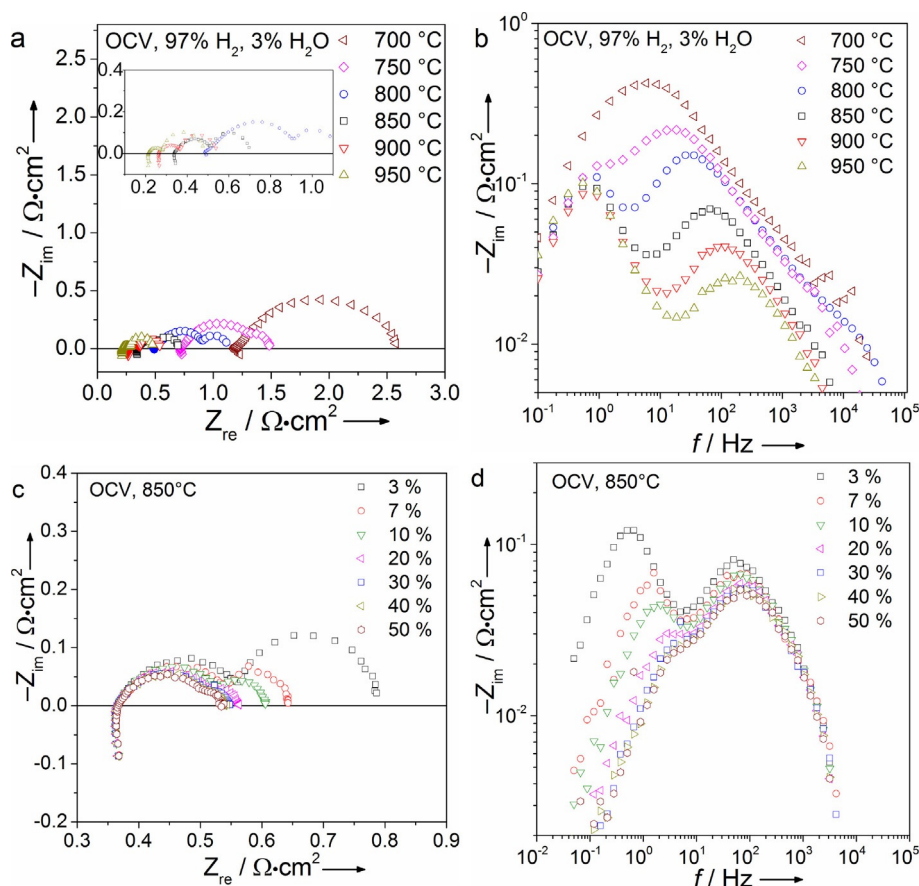
Figure 2. a) Nyquist and b) imaginary impedance plot of impedance spectra of a Ni/CGO40-based SOFC recorded at $T = 700$ –950 °C, OCV, pO$_2 = 0.21$ atm, and pH$_2$O $= 0.03$ atm, c) Nyquist and d) imaginary impedance plot of impedance spectra of the cell recorded at $T = 850$ °C, OCV, pO$_2 = 0.21$ atm, and pH$_2$O $= 0.03$–0.5 atm.

mately 50 Hz (Figure S5). The influence of the changing water partial pressure at 10^1–10^2 Hz on the imaginary impedance plot presented in Figure 2d indicates clearly the existence of an anode surface process. The intensity of the peak of this anode process is decreased and its characteristic frequency peak is slightly shifted to higher values with increasing pH_2O, which reflects the decreasing process resistance caused by the enhanced kinetics. Although this seems to be counterintuitive, a similar enhancing effect of the increasing pH_2O on H_2 oxidation kinetics has already been observed for Ni/YSZ anodes caused by the participation of H_2O as a reactant in one of the rate-limiting steps.[43] This indicates a similar role of H_2O in the oxidation mechanism of Ni/CGO40-based anodes.

The existence of an anode surface process at approximately 100 Hz is contrary to the results shown in Figure 1d for a Ni/CGO10-based cell, which did not show a significant influence of water in this frequency range. This gives rise to the assumption that the same anode surface process appears in completely different frequency ranges for different cells. In symmetrical cell measurements of Ni/CG40 anodes with a similar design as that in the present study, Iwanschitz et al. observed two anode processes: one middle-frequency process between 50–100 Hz and one low-frequency process at 1–2 Hz.[22] Although they admit that gas conversion could contribute to the low-frequency process, on the basis of the observation that redox cycling was observed to have an effect on this process and a comparison to other literature sources, they interpreted it as an actual electrode process rather than a gas transport process. In the presented study, upon a decrease of temperature, a small effect on the low-frequency impedance spectra is visible by a peak shift to higher frequencies at 750 °C (Figure 2). However, the increase of pH_2O in the fuel gas leads to a stepwise decrease of the intensity of the low-frequency peak shown in Figure 2d, which displays the typical behavior of a gas conversion process. At a humidity level of 0.3 atm, the low-frequency peak has nearly disappeared. To better deconvolute the gas conversion and the low-frequency anode process observed previously, the fuel gas flow rate was decreased from 1 to 0.2 L min^{-1}. Additionally, at this comparatively low specific fuel gas flow rate, the pH_2O was varied between 0.15 and 0.5 atm. The impedance spectra recorded at the respective operating conditions are shown in Figure 3. Both the Nyquist plot shown in Figure 3a and the imaginary impedance plot shown in Figure 3b indicate the presence of more than one semicircle in the low-frequency arc, which points towards the existence of another low-frequency process in addition to gas conversion. This is further confirmed by the calculated distribution of relaxation times (DRT) presented in Figure 4c, which shows the existence of one process at 0.3 Hz and another one at 0.02 Hz at 0.15 atm, both of which are dependent on the humidity. This underlines the difficulties associated with their assignment to a specific process. However, as a reduction of the fuel gas flow rate generally results in a shift of the gas conversion process to lower frequencies, the process at 0.02 Hz is suggested to be caused by gas conversion. This implies that the process at 0.3 Hz is an anode process as suggested by Iwanschitz et al.[22] In the present study, the same anode
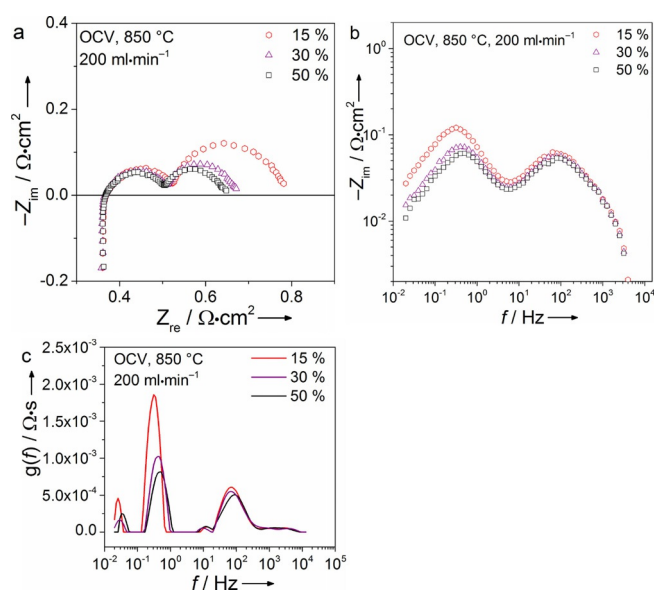
Figure 3. a) Nyquist and b) imaginary impedance plot of impedance spectra of a Ni/CGO40-based SOFC recorded at $T = 850$ °C, OCV, $pO_2 = 0.21$ atm, 200 mL min^{-1}, and $pH_2O = 0.15$–0.5 atm. c) Calculated DRT.
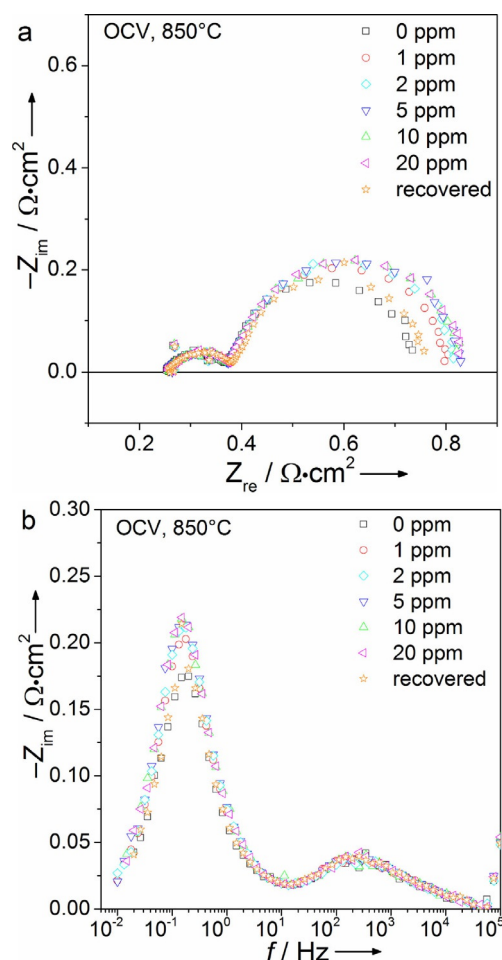
Figure 4. a) Nyquist and b) imaginary impedance plot of impedance spectra of cell A recorded at $T = 850$ °C, OCV, $pO_2 = 0.21$ atm, $pH_2 = 0.97$ atm, $pH_2O = 0.03$ atm, and H_2S concentrations of 0–20 ppm.

design was used as in the work of Iwanschitz et al., except for the addition of small amounts of Cu in the metallic phase. The observation of anode processes at the same frequency in the impedance spectra is strong evidence that the influence of Cu on the hydrogen oxidation mechanism is negligible. However, the alloying of Ni with Cu has been shown to lower the sulfur adsorption energy for $Ni_{0.5}Cu_{0.5}$.[44,45] Thus, although the amount of Cu in the present study is small, a minor influence of Cu on the magnitude of the sulfur-poisoning-related resistance increase cannot be excluded.

In summary, two low-frequency processes could be identified in the impedance spectra of cell B as well. However, in contrast to that observed for cell A, the middle-frequency process is affected by humidity, and therefore, is assigned to a surface process. Additionally, one low-frequency process with an unclear origin was observed. No bulk anode process in the middle-frequency range was observed, however, because of the possible convolution of processes in this region, its existence cannot be excluded.

Sulfur poisoning

In the following subsection, the systematic investigation of sulfur poisoning of the two different anodes is presented. To facilitate the comparison of the poisoning behavior of each cell under the different operating conditions, all sulfur poisoning experiments were conducted with the same cell, as this approach avoids problems with regard to slightly different performance, tightness, and contacting. As the sulfur poisoning behavior on Ni/CGO anodes is expected to be mainly reversible, this approach should be viable (vida infra). To avoid sulfur-related irreversible degradation, after the saturation of the respective performance drop was reached, the poisoning intervals were kept as short as possible.

Sulfur poisoning of Ni-CGO10-based anodes

The voltage stability tests over time are depicted in Figure S6 for temperature variations between 800 and 900 °C at 0.5 A cm^{-2} and for current density variations at constant $T =$ 850 °C between the open-circuit voltage (OCV) and 0.75 A cm^{-2}. In all cases, the overall voltage drop is stepwise and increases with the H_2S concentration. The initial performance drop associated with the exposure of 1 ppm H_2S is the largest, and a further increase of the H_2S concentration only leads to smaller performance losses. For the exposure times investigated in the present study, full recovery was reached within 22 h after the sulfur supply was switched off at all operation points.

As the introduction of H_2S did not lead to a voltage drop at the OCV, the poisoning characteristics were captured by using impedance spectroscopy. The corresponding recorded spectra are illustrated in Figure 4. Although sulfur exposure has no influence on the identified bulk processes in the middle-frequency region, it leads to an increase in the low-frequency arc associated with an influenced frequency range at around 0.1 Hz, which is consistent with the identification of an anode surface

process at this frequency in Figure 1. This value is approximately four orders of magnitude lower than the peak frequencies observed commonly for Ni/YSZ-based SOFC ($\sim 10^3$–10^4 Hz) that display an electric double layer capacitance at the interface between the electrolyte (YSZ) and electrode (Ni).[2,6,46] Thus, as a result of the large shift in the relaxation frequency, it can be concluded that the capacitance of the observed Ni/CGO10 anode process has a different nature to that of Ni/YSZ anodes, which indicates fundamental differences in the underlying hydrogen oxidation mechanisms. The low frequency of the observed anode surface process is in good agreement with the frequency of Ni/CGO10 electrode processes reported previously.[24,39] Furthermore, the low-frequency surface process is consistent with reports of the frequencies of Ni-free CGO10 and CGO20 electrodes.[21]

In these studies, the nature of the low-frequency process was related to hydrogen oxidation on the CGO surface that causes a surface/gas-phase double layer, which in turn leads to an electrostatic potential step between surface and bulk. Gd-doped ceria is characterized by the occurrence of a chemical capacitance similar to other MIECs.[47,48] At the MIEC surface, a double layer is created by the accumulation of electronic charges in the space–charge layer near the MIEC surface (here Ce^{3+}) and ions adsorbed on the surface (here OH^-).[29] Thus, a changing electrode potential is reflected by a simultaneous change in the concentration of the electrochemically relevant adsorbants and Ce^{3+}/Ce^{4+} ratio as a result of the following global reaction [Eq. (1)]:

$$2\,Ce_{Ce}^{x} + O_O^{x} + H_2 \rightleftharpoons 2\,Ce_{Ce}' + V_O^{\bullet\bullet} + H_2O \tag{1}$$

in which the species in the Kröger–Vink notation are Ce^{4+}, O^{2-}, Ce^{3+}, and the oxygen vacancy from left to right. Feng et al. investigated samaria-doped ceria (SDC20) at 500 °C and proposed the electron transfer between the OH^- intermediate and Ce^{4+} to be the rate-limiting step that can be expressed as [Eq. (2)]:

$$Ce_{Ce}' + OH_O^{\bullet} \rightleftharpoons Ce_{Ce}^{x} + OH_O^{x} \tag{2}$$

in which $OH_O^{\bullet}$ sits on the surface oxygen vacancy site.[19] Thus, surface reduction leads to an increasing number of oxygen vacancies on the surface and a higher Ce^{3+} concentration.[49] Thus, the mixed-valence Ce^{3+}/Ce^{4+} is responsible for the large chemical capacitance. This capacitance, in turn, could possibly be coupled to hydrogen dissociation on Ni to explain the low-frequency influence of sulfur poisoning.

Influence of current density and temperature

Recent studies on the sulfur poisoning of Ni/YSZ have demonstrated the difficulties to find an appropriate descriptor to quantify the extent of sulfur poisoning in full-cell measurements as cathode and gas diffusion/concentration resistance contributions might superimpose the anode poisoning behavior.[5,50,51] As it was not possible to deconvolute the anode surface process from the gas conversion process at low frequen-

cies to calculate the relative resistance increase upon poisoning, in the presented study we employed the absolute decrease in voltage and the absolute increase of the total area-specific cell resistance (ASR) to evaluate the extent of sulfur poisoning. The values of the voltage drops depicted in Figure 5 a show the same characteristic behavior for all current densities with a sharp drop for low H_2S concentrations and a saturation effect at higher concentrations. This strongly resembles the saturation effect also observed for Ni/YSZ, which was related to the saturation of S on the Ni surface.[2, 52, 53] The sulfur coverage on Ni can be estimated by using a Temkin isotherm as shown by Alstrup et al.[54] The respective calculated values for the conditions employed in the present study are depicted on the right y axis in Figure 5 a. The behavior of the sulfur coverage on Ni and the voltage drop is indeed strikingly similar, which indicates that the observed Ni/CGO sulfur poisoning could be caused by Ni surface poisoning. This is consistent with previous studies in which Ni infiltration enhances the same low-frequency process as the sulfur poisoning of CGO slows down.[25, 34]

Contrary to earlier reports on the sulfur poisoning of Ni/CGO anodes, the voltage drops in the present study demonstrate that the sulfur poisoning of Ni/CGO-based anodes can affect SOFC performance significantly.[8, 10, 11] A comparison of the different curves presented in Figure 5 reveals that increasing current densities lead to higher drops in performance. Although this behavior itself is not surprising, the increase of ASR observed in Figure 5 b shows the opposite behavior and indeed indicates some kind of mitigation effect at high current densities. However, interestingly, the increased ASR values for the

experiments at the OCV are not in accordance with this trend as they are significantly smaller than the ASR increase values for 0.25 $A\,cm^{-2}$. Although we cannot explain this behavior, it could be reproduced with different cells of the same type.

Previous investigations of sulfur poisoning of Ni/YSZ anodes revealed that the relative increase in ASR tends to decrease with increasing polarization, which gives rise to the hypothesis that large oxygen ion flows lead to a reduced sulfur surface coverage on Ni by a S oxidation reaction to SO_2.[50] However, recent studies have suggested the converse behavior.[2, 5, 7] Thus, the observed mitigation effect might be related to improved anode kinetics because of increased humidity levels in the anode compartment rather than to the actual sulfur oxidation to SO_2 and its subsequent removal from the anode surface. Furthermore, the increase of the ASR values for the OCV experiment are lower than at an applied current density of 0.25 $A\,cm^{-2}$, which is inconsistent with the hypothesis of SO_2 formation. Nonetheless, recent DFT calculations of sulfur oxidation on doped ceria surfaces showed that sulfur oxidation to SO_2 displays favorable kinetics as surface lattice oxygen could be used to oxidize the ceria-adsorbed sulfur.[55]

The same trend of a lower voltage drop and a lower ASR increase with the increasing temperature are shown in Figure 5 c and d, which indicates a mitigating effect of the temperature on the extent of sulfur poisoning. A similar behavior has also already been observed for the sulfur poisoning of Ni/YSZ and was related to an increasing desorption of H_2S from the Ni surface with increasing temperature and, consequently, a reduced sulfur surface coverage.[56] This could also be the case in the present study, as desorption processes are generally endothermic and, hence, energetically more favorable with increasing temperature.

The observed voltage drops for higher H_2S concentrations at 800 °C reach values of over 100 mV. These voltage drops already approach the magnitude of values observed for Ni/YSZ.[52] This is a lot more severe than that in earlier studies of Ni/CGO10 anodes.[8, 10] The reason for the significantly larger performance drops in the present study are so far unclear. However, they indicate that the microstructure of Ni/CGO anodes plays an important role to determine the sulfur tolerance of such electrodes.

The differential imaginary impedance spectra presented in Figure 6 a confirm the behavior observed in Figure 5 d with a more pronounced increase of the imaginary impedance at higher temperatures after the exposure of the anode to 1 ppm H_2S. Interestingly, however, the peak frequency of the differential impedance spectra increases with decreasing temperature, which implies that the characteristic frequency of the low-frequency anode surface process changes as well. As indicated earlier, this is rarely observed for SOFC as thermally activated processes generally exhibit higher resistances at lower temperatures and cause the corresponding characteristic frequencies to shift to lower values. Hence, the observed behavior must be caused by a significant decrease of capacitance with decreasing temperature. This is also confirmed by the results of a complex nonlinear least-squares (CNLS) fit of a reduced equivalent circuit model (ECM) to the experimental data. The ECM is de-
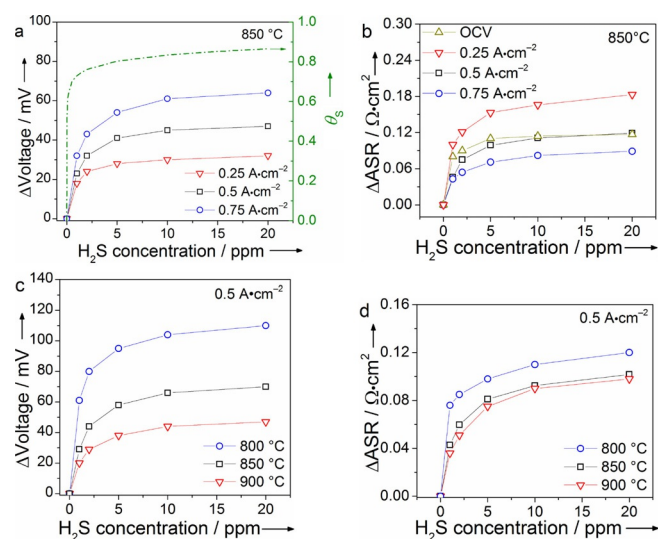
Figure 5. a) Accumulated voltage drop and b) accumulated total resistance increase at $T=850\,°C$, $pO_2=0.21$ atm, $pH_2=0.97$ atm, and $pH_2O=0.03$ atm as a function of H_2S concentration at different current densities. c) Accumulated voltage drop and d) accumulated ASR increase at a current density of 0.5 $A\,cm^{-2}$, $pO_2=0.21$ atm, $pH_2=0.97$ atm, and $pH_2O=0.03$ atm as a function of H_2S concentration at different temperatures. The right y axis in a) shows the calculated sulfur coverage on Ni according to the Temkin isotherm derived in Ref. [54]. The experiments in c) and d) were conducted with a different cell from the same batch as the cell tested for a) and b). Thus, the values do not coincide completely.
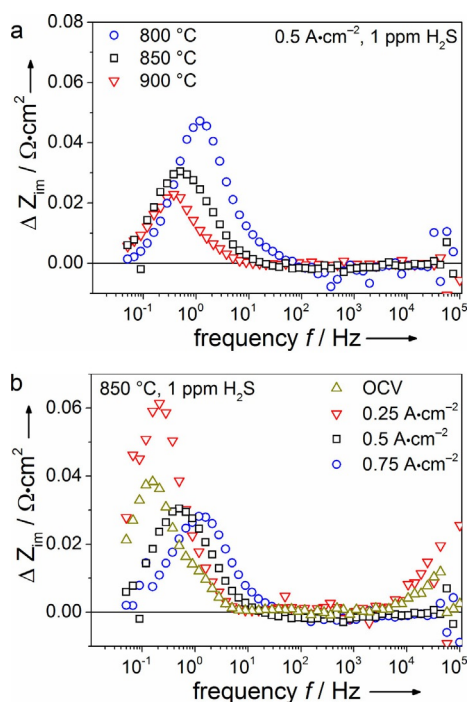
Figure 6. Differential impedance spectra (subtraction of imaginary impedance of 0 ppm H_2S spectra from 1 ppm H_2S) for a) different temperatures at constant $i = 0.5\ A\,cm^{-2}$ and b) different current densities at constant $T = 850\,°C$.

picted in Figure S7, and the corresponding results are shown in Table S1.

A similar analysis can be performed based on the differential impedance spectra for varying current densities (Figure 6 b). The peak intensities confirm the trends observed in Figure 5 b, and the test at 0.25 A cm^{-2} is the most severely poisoned by 1 ppm H_2S. Again, it is interesting to see that the increase in current density leads to a peak frequency shift from 0.1 Hz at OCV to 1.4 Hz. Although a certain shift to higher frequencies can be expected because of the possibly accelerated kinetics at higher $p H_2O$, a shift of more than one order of magnitude is comparatively large.[57] Moreover, although it is well known that double layer capacitances can be dependent on temperature and gas composition,[58] this influence is negligible in many cases and they are frequently assumed to be constant.[38,43] However, the present results suggest that the chemical capacitance of the surface anode process that leads to hydrogen oxidation on Ni/CGO10 is highly dependent on both parameters. As mentioned already, the chemical capacitance of the anode surface process is caused by the mixed-valence Ce^{3+}/Ce^{4+}. Recently, it has been shown that the Ce^{3+} surface concentration in CGO is almost independent of temperature and oxygen activity, however, the Ce^{3+} bulk concentration increases considerably with increasing temperature and decreasing $p O_2$, which is consistent with the capacitance changes observed in the present work.[18,20,59] This could indicate that the chemical capacitance of Ni/CGO10 is not only constrained to the surface but further extended into the bulk.

Sulfur poisoning of Ni/CGO40-based anodes

In the following, the electrochemical results for the sulfur poisoning of cell B are presented with a systematic variation of current density and temperature as described earlier. All sulfur poisoning experiments are shown in Figure S8. The overall poisoning behavior of cell B resembles that of cell A strongly with a significant voltage drop after exposure to 1 ppm H_2S and a subsequent saturation of the voltage drop. However, although the regeneration of cell B between 850 and 950 °C leads to a complete voltage recovery under all operating conditions, this is not the case at 800 °C (Figure S8 b). At this operating temperature, the voltage stabilizes after approximately 20 h of poisoning, but at a value 10 mV lower than the initial one. This demonstrates that sulfur exposure can cause irreversible degradation on Ni/CGO anodes. As this irreversible degradation behavior could not be observed at any other operation point and as the investigation at 800 °C was conducted last in the present study, the most likely explanation for this behavior is that the onset of irreversible degradation is reached after a certain time of operation. More carefully planned long-term experiments under varying conditions will be required to confirm this hypothesis.

Impedance spectra at the OCV are affected by sulfur exposure by an increase of the higher-frequency arc in the Nyquist plot at a frequency range between 10^1 and 10^2 Hz (Figure 7). The plots of the initial and the recovered impedance spectra overlap at each recorded frequency point, which indicates a full recovery also at the OCV. The low-frequency range of the spectra remains unaltered, which indicates the absence of an anode surface process. Interestingly, the frequencies of the impedance spectra affected by sulfur are more than two orders of magnitude higher than those for cell A, which indicates significant differences between the behavior of Ni/CGO10- and Ni/CGO40-based anodes. However, the affected process is still at a frequency 2–3 orders of magnitude lower than that of Ni/YSZ, which is caused by the double layer capacitance at the interface between Ni and YSZ.[2,7] Although the peak frequency of the affected process is significantly higher for cell B than for cell A, the overall sulfur poisoning behavior remains similar both in regard to the magnitude of the performance drops and their evolution with H_2S concentration and current density. Under the assumption that the resistances of both anode processes are approximately the same, the capacitance of the sulfur-affected process for the Ni/CGO40-based anode can be estimated to be twice that of Ni/CGO10. SEM pictures of the respective anodes are shown in Figure 8. The microstructure of cell B is finer and less porous than that of cell A. This could lead to an increased TPB length and a faster charge-transfer reaction and could, furthermore, be reflected by a shift of the anode charge-transfer reaction to higher frequencies. However, as a result of the similarity of the performance with respect to the i–V curves (Figures S2 and S4) and the polarization resistances derived from impedance measurements (e.g., Figures 4 a and 7 a), we do not expect a frequency shift as high as two orders of magnitude. However, a minor influence of the different microstructures cannot be excluded.
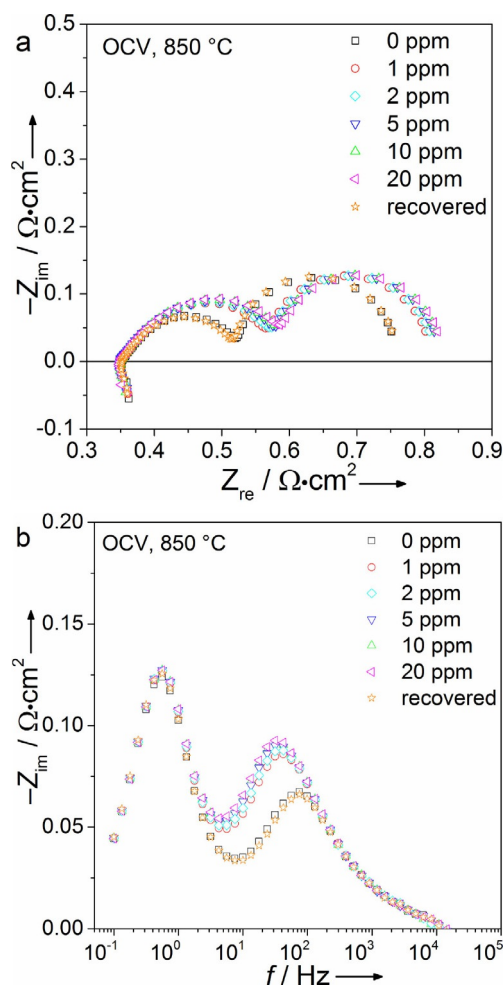
Figure 7. a) Nyquist and b) imaginary impedance plot of impedance spectra of cell B recorded at $T = 850\,°C$, OCV, $pO_2 = 0.21$ atm, $pH_2 = 0.97$ atm, and $pH_2O = 0.03$ atm with different H_2S concentrations of 0–20 ppm.

Figure 8. SEM cross-section image of the anodes of reference cells A (top) and B (bottom).

Previously, it has been shown that the amount of Ce^{3+} in CGO is affected by the Gd-doping concentration as the introduction of a trivalent dopant enhances the stability of Ce^{4+}.[60] It has also been reported that Gd doping higher than 25% could lead to the surface segregation of the Gd phase and, consequently, to a more tortuous Ce network within the CGO phase.[61] This is reflected by a significantly lower electronic conductivity of CGO at higher Gd contents.[60] Thus, as the capacitance of CGO is determined by the amount of available Ce^{3+}, this value can be expected to be significantly lower for CGO40 than for CGO10, which leads to a substantial shift of the surface process to higher frequencies in the impedance spectra. Although similar relaxation frequencies impede the direct separation of the anode surface process, the results of equivalent circuit modeling summarized in Table S2 confirm the significantly lower capacitance value in the case of the CGO40-based anode (~ 100 mF, compared to ~ 1 F for Ni/CGO10). This large shift in capacitance could also be interpreted to be caused by a reduced electrochemically active region on CGO40.[62]

In their attribution of the low-frequency peak of Ni/CGO40 to a charge-transfer process, an important argument in the

work of Iwanschitz et al. is the comparison to other experimental data published previously, among which are many studies based on Ni/CGO anodes with a lower Gd content.[22] Although this process was also observed in the present work (Figure 3), it is not affected visibly by sulfur exposure, which makes a charge-transfer process as its origin unlikely. Throughout the last sections it was shown that the anode surface process observed at frequencies around 0.1 Hz in Ni/CGO10 anodes is observed at significant higher frequencies for Ni/CGO40-based anodes.

Thus, it can be concluded that the impedance spectra of Ni/CGO anodes with different Gd contents have to be handled with caution as processes might be subject to significant frequency shifts, which can lead to misinterpretations. The physicochemical origin of the observed low-frequency process in Ni/CGO40 anodes and if it is present in Ni/CGO10-based anodes so far remains unclear. It could possibly be related to a surface diffusion process as suggested previously.[24]

Influence of current density and temperature

To compare the dependence of the degradation behavior on the current density, voltage drops and ASR changes are depicted over the imposed H_2S concentrations in Figure 9 a and b. Furthermore, the influence of temperature is shown in Figure 9 c and d. All curves show a similar characteristic saturation behavior as in Figure 5, which indicates that the underlying poisoning mechanism is probably the same. Similar to that shown in Figure 5, the increasing current density shows a mitigating effect on the sulfur poisoning behavior, which is reflected by a decreasing ASR increase with current density. In con-
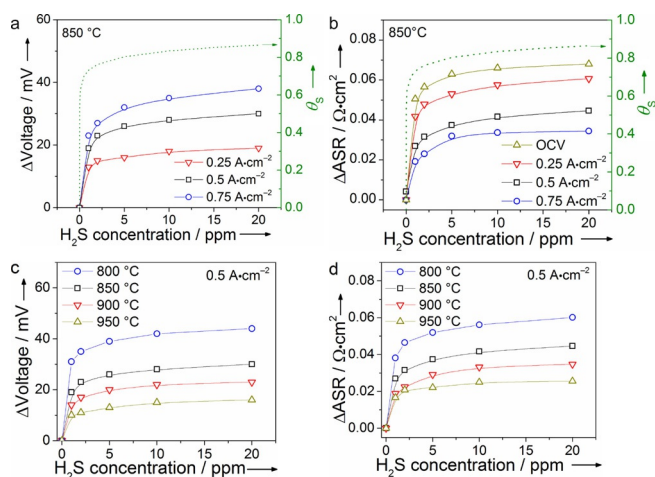
Figure 9. a) Accumulated voltage drop and b) accumulated ASR increase at $T = 850\,°C$, OCV, $pO_2 = 0.21$ atm, $pH_2 = 0.97$ atm, and $pH_2O = 0.03$ atm as a function of H_2S concentration at different current densities. c) Accumulated voltage drop and d) accumulated ASR increase at a current density of $0.5\ A\ cm^{-2}$, OCV, $pO_2 = 0.21$ atm, $pH_2 = 0.97$ atm, and $pH_2O = 0.03$ atm as a function of H_2S concentration at different temperatures. The right y axes in a) and b) show the calculated sulfur coverage on Ni according to the Temkin isotherm derived in Ref. [54].

Figure 10. Differential impedance spectra (subtraction of imaginary impedance of 0 ppm H_2S spectra from 1 ppm H_2S) for a) different temperatures at constant $i = 0.5\ A\ cm^{-2}$ and b) different current densities at constant $T = 850\,°C$.

trast to that shown in Figure 5, even the increased ASR values for the OCV experiments obey this trend.

The same trend of a lower voltage drop and a lower ASR increase with increasing temperature are shown in Figure 9 c and 9 d analogous to the behavior of cell A shown in Figure 7. The increasing sulfur desorption could also occur for sulfur surface poisoning of the CGO surface, which was confirmed by using a combined TPD and XPS analysis by Mullins and McDonald.[35] In that study the adsorption and dissociation of hydrogen sulfide was investigated on reduced ceria surfaces that resemble a gadolinia-doped ceria surface with regard to their high Ce^{3+} surface concentration to show that the sulfur coverage decreases with temperature. Even for temperatures as high as 700 °C, the authors could detect sulfur on the reduced ceria surface. However, they also mention that above 500 °C sulfur could diffuse into bulk ceria to lower the surface coverage, which could possibly give rise to long-term degradation effects. The incorporation of sulfur into the CGO10 bulk phase at 10 ppm H_2S exposure was also shown recently to be higher at increased temperatures by using time-of-flight secondary ion mass spectrometry (TOF-SIMS).[63] In the present study, by using energy-dispersive X-ray spectroscopy (EDX), we were not able to detect any traces of sulfur postmortem. Thorough long-term experiments will be required to shed more light on the sulfur–CGO interactions in SOFC operation.

The behavior observed in Figure 9 is conformed in Figure 10, with a more pronounced increase of the imaginary impedance at higher temperatures and lower current densities. In contrast to that of the Ni/CGO10-based cells, however, the peak frequencies of the differential impedance spectra decrease with decreasing temperature to exhibit behavior observed typically for thermally activated processes. Furthermore, the change from OCV conditions to $0.75\ A\ cm^{-2}$ leads to
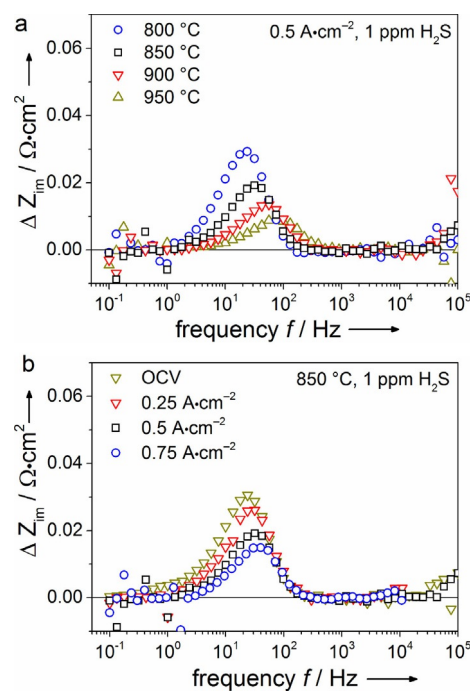
a peak frequency shift from 23 to 37 Hz, which is a lot smaller than that observed in Figure 6. This is an indication that, in contrast to that of Ni/CGO10, the capacitance of the anode surface process on the Ni/CGO40-based anode is significantly less dependent on temperature and the gas-phase composition.

Influence of H_2S on the fuel oxidation mechanism in Ni/CGO-based anodes

Although early investigations of the sulfur poisoning of Ni/CGO and Ni/YSZ anodes concluded both anodes to have the same underlying sulfur poisoning mechanism, recently, the reason for the high sulfur tolerance of Ni/CGO was explained to originate from its MIEC characteristics.[8, 10, 11] Several studies have suggested that Ni primarily assumes the role of a pure electronic conductor in Ni/CGO anodes, which improves the comparatively low electronic conductivity of CGO and extends the electrochemical reaction zone to the gas–ceria interface.[17] According to these studies, the sulfur adsorption on the Ni surface would not be expected to have a major influence on SOFC performance, which is in contrast to the sulfur poisoning behavior presented in this work. However, recently, it was confirmed experimentally that pure CGO anodes can be poisoned by sulfur as well to lead to the same characteristic performance drops as for Ni/CGO composite electrodes.[34] Furthermore, computational ab initio studies have shown that H_2S can dissociate on the ceria surface to create elemental sulfur that blocks the active surface area.[64] Probably, the observed sulfur poisoning of Ni/CGO anodes is a convolution of the sur-
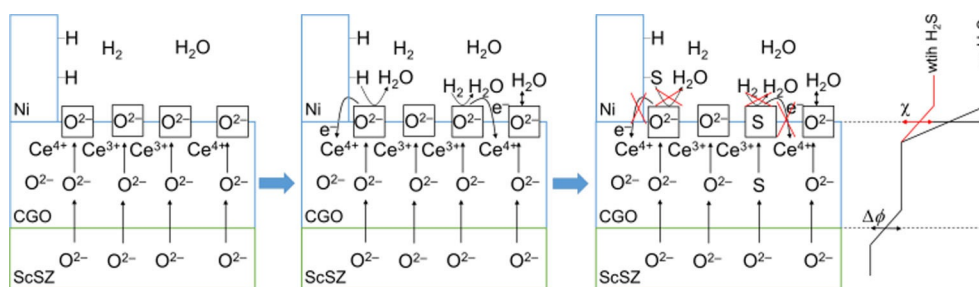
Figure 11. Illustration of the reaction mechanism of fuel oxidation and sulfur poisoning mechanisms in Ni/CGO-based anodes of a SOFC. The first block represents the general initial configuration of Ni/CGO anodes, the second block shows the normal operation upon exposure to H_2/H_2O, the third block shows the influence of sulfur on the (electro-)chemical processes, and the fourth diagram demonstrates the potential drop at different interfaces. All structural details and scaling are exaggerated for illustration purposes.

face poisoning of both the Ni and CGO surfaces as illustrated in Figure 11. Moreover, previously, sulfur atoms were observed in the CGO bulk phase, which could indicate a mitigating effect of sulfur diffusion on the poisoning behavior.

Although the impedance spectra of Ni/CGO10- and Ni/CGO40-based anodes exhibit significant differences, the similarity of their sulfur poisoning behavior leads us to the conclusion that their underlying mechanisms are probably the same. The large differences in the capacitance of the identified anode surface processes are likely to be caused by the lower availability of Ce^{3+} and thus possibly, a reduced electrochemically active region on CGO40. As it is outlined above, fuel oxidation on Ni/CGO-based anodes of SOFC proceeds essentially through the so-called bulk-surface path, in which oxygen anions first migrate through the electrolyte/electrode boundary (YSZ/CGO) and then through the electrode–bulk/electrode–surface interface (CGO–bulk/CGO–surface).[28] Finally, at the surface of CGO, oxygen atoms are oxidized by hydrogen to form H_2O. Hydrogen can be dissociated on Ni and supplied to CGO by a spillover mechanism, or alternatively could be dissociated and oxidized on CGO directly. Oxidation could also occur on CGO through a Mars–van Krevelen mechanism as suggested for CO oxidation on ceria catalysts.[65] Although all of these mechanisms could be competitive, it is likely that the dominant mechanism depends on the microstructure of the respective electrode. This is supported by the considerable differences between the voltage drops observed in the present study and the values reported previously. As shown above, sulfur adsorbs both on the Ni and the CGO surfaces and blocks active surface sites of the electrode to deteriorate fuel oxidation. As a result, the electrostatic surface potential step (χ), shown in red in Figure 11, diminishes. The interfacial potential step ($\Delta\phi$) seems to stay constant during our experiments, which indicates the lack of significant influence of sulfur on the CGO bulk-surface transport for the exposure times investigated. As both hypotheses (sulfur poisoning of Ni and CGO) are supported by a substantial amount of studies, a clear mechanistic explanation cannot be given within the framework of the present study. To further investigate the role of Ni during the sulfur poisoning of Ni/CGO anodes, more careful electrochemical poisoning measurements on SOFC with various compositions of the metallic phase (Ni, Cu, Au) could be helpful.

Conclusions

This work aims to advance the understanding of the electrochemical processes that occur during the sulfur poisoning of Ni/gadolinium-doped ceria (CGO) based anodes. Therefore, electrolyte-supported Ni/CGO10- and Ni/CGO40-based solid oxide fuel cells (SOFC) were characterized extensively by analyzing their current–voltage curves and impedance spectra. Moreover, the short-term sulfur poisoning behavior of the SOFC was investigated systematically under a wide range of operating conditions at various temperatures and current densities in H_2/H_2O fuels with different H_2S concentrations (1–20 ppm). The investigated cells showed performance losses of up to 100 mV, which is considerably higher than that reported previously and demonstrates a possibly considerable effect of the microstructure of Ni/CGO anodes on sulfur tolerance. The analysis of the area-specific cell resistance increase displayed a sulfur mitigation effect at high current loads and temperatures. The poisoning behavior was shown to be reversible for short exposure times. The sulfur poisoning behavior of the different anodes was observed to be similar in both the magnitude of the cell voltage drops and the saturation behavior. However, the analysis of comparable impedance spectra revealed that the sulfur-affected processes can be found at substantially different relaxation frequencies that depend on the Gd-doping level of the CGO-based anode. Ni/CGO40-based anodes were affected at frequencies of approximately 50 Hz, whereas the impedance spectra of the Ni/CGO10-based anodes showed an increase at 0.1 Hz. Moreover, the capacitance of the anode surface process in Ni/CGO10 was shown to exhibit a significant dependence on both the operating temperature and gas-phase composition, which reflects a changing Ce^{3+} concentration in CGO, although this was not the case for Ni/CGO40-based anodes. From these differences, it could be demonstrated that the capacitance of Ni/CGO-based anodes is strongly dependent on multiple parameters and thus, a direct comparison between the impedance spectra of different Ni/CGO-based anodes, which is performed frequently in the literature, should be avoided.

Although the observed reversible degradation and voltage drops are encouraging with regard to the operation of Ni/CGO anodes with sulfur-containing H_2/H_2O fuel gases, further research efforts should be devoted to the investigation of sulfur

poisoning in reformate-operated Ni/CGO-based SOFC. To gain a deeper understanding of the mechanism of Ni/CGO, symmetrical cell measurements on a laboratory scale should be designed to avoid the convolution of the anode processes with cathode and/or gas conversion processes.

Experimental Section

Two different kinds of electrolyte-supported SOFC (ESC, hereafter named as cell A and cell B) were investigated, both based on 160 µm thick Sc-stabilized zirconia (ScSZ) electrolytes and 65 µm thick LSM/ScSZ cathodes. Cell A is a commercial SOFC with a Ni/$Ce_{0.9}Gd_{0.1}O_{2-\delta}$ (CGO10) anode manufactured by Kerafol. Cell B was produced and provided by Hexis with a NiCu5/$Ce_{0.6}Gd_{0.4}O_{2-\delta}$ (CGO40) anode. The weight ratio between the metallic and ceramic phase was 50:50 in both cases. Cell A employed 10Sc1CeSZ as the electrolyte and the active cathode layer. The composition of the LSM was $(La_{0.75}Sr_{0.25})_{0.95}MnO_3$. The weight ratio between LSM and ScSZ in the composite electrode was 50:50. Cell B consisted of a 6ScSZ electrolyte and an $(La_{0.75}Sr_{0.25})_{0.95}MnO_3/8YSZ$ cathode. SEM images of polished cross-sections of the anodes of cells A and B, both 25 µm thick, were recorded by using a Zeiss Ultra Plus SEM and are shown in Figure 8. Cell A employed an additional 5 µm thick CGO10 adhesion layer between the electrolyte and functional anode layer. In cell B the functional anode layer was applied directly onto the electrolyte. Furthermore, in both cells a current collector layer with an increased Ni content was utilized. The use of Cu as an anode material is known to entail a higher carbon and sulfur tolerance.[32] It has been reported that in Cu-ceria composite electrodes, the metal phase is simply an electronic conductor and does not play a catalytic role.[66,67] Moreover, Cu only accounts for 5 wt% of the metallic phase. Although minor effects on the extent of sulfur poisoning cannot be excluded, the influence of Cu on the general sulfur poisoning behavior of cell B is assumed to be negligible. In any case, also because of different processing conditions and microstructure, this work only presents a qualitative comparison of the cells. The active area of the planar cells was 4×4 cm² with a total area of 5×5 cm². The experimental setup in which the cells were tested to enable the characterization of up to four cells simultaneously is shown in Figure S1. This rather unusual configuration provides some important advantages compared to other test rigs. In particular, important parameters for fuel cell characterization, such as current density and sulfur concentration in the fuel gas can be varied simultaneously from cell to cell in the same experiment to establish a detailed experimental map of SOFC performance and durability. The testing cells were placed in the reaction chamber (ceramic cell housing; Figure S1b) in which the anode and the cathode were contacted with Ni and Pt meshes, respectively, and Au was employed as the sealant between the anode and the cathode side. In addition, thermocouples (TC) were positioned just next to the respective electrode in the center of the channel rib. Unless stated otherwise, the cells were operated with various H_2/H_2O fuel mixtures and different H_2S concentrations at a constant total fuel flow rate of 1 L min^{-1} for each cell. The cathode was operated with air with a constant flow rate of 2 L min^{-1}. Humidification was performed by running the gas through a temperature-controlled water bubbler. H_2S was taken from a pressurized H_2S/H_2 bottle that contained 100 ppm H_2S. To avoid sulfur adsorption on the piping and its dissolution in the water bubbler, the sulfur was injected into the fuel stream only 6 cm away from the cell housing and Teflon-coated tubing was used. The cells were heated briefly (3 K min^{-1}) to 950 °C for sealing and, subsequently, the temperature was reduced to 900 °C. An ini-

tial cell characterization was performed by measuring cell voltage curves as a function of current density (i–V curves) and by recording electrochemical impedance spectra (EIS) at different temperatures and with a series of different gas compositions fed to the anode and cathode, respectively. The i–V curves and impedance spectra were measured between 650 and 950 °C (800–950 °C for cell B) at steps of 50 K and pH_2/pH_2O (97:3) mixtures. Furthermore, impedance spectra were recorded at different pH_2O between 0.03 and 0.5 atm. Subsequently, the temperature was set to 850 °C, and sulfur poisoning experiments were conducted at different current densities. The investigated current densities were 0.5, 0.75, 0.25 A cm^{-2}, and OCV in this order. In addition, the operating temperature was varied to 900, 950 (only for cell B), and 800 °C, and poisoning experiments were performed at 0.5 A cm^{-2}. For cell A, the poisoning experiments at 800 and 900 °C were performed by using a different cell of the same specifications from the same batch. Additionally, the experiment at 850 °C with 0.5 A cm^{-2} current density was repeated with this cell. The poisoning experiments were performed for a H_2/H_2O ratio of 97:3. For a systematic investigation of the sulfur poisoning behavior the H_2S concentration was increased stepwise and set to 1, 2, 5, 10, and 20 ppm at each operating point until saturation occurred. After the saturation of the last performance drop related to 20 ppm H_2S, the supply of H_2S was switched off, the gas flow was substituted with pure H_2, and the anode was regenerated until the full recovery of the SOFC performance was achieved. Unless stated otherwise, the cells were characterized by using EIS by using an electrochemical workstation (Zahner® PP-240 with Thales software) in the frequency range from 100 mHz to 100 kHz with 8 points decade^{-1}. The amplitude of the current stimulus was chosen to achieve a voltage response not higher than 15 mV. The DRT was calculated by using a modified Levenberg–Marquardt algorithm adapted from Ref. [68].

[1] R. Kee, H. Zhu, *Combust. Sci. Technol.* **2008**, *180*, 1207.
[2] M. Riegraf, G. Schiller, R. Costa, K. A. Friedrich, A. Latz, V. Yurkiv, *J. Electrochem. Soc.* **2015**, *162*, F65.
[3] A. Hagen, J. F. B. Rasmussen, K. Thydén, *J. Power Sources* **2011**, *196*, 7271.
[4] A. Hauch, A. Hagen, J. Hjelm, T. Ramos, *J. Electrochem. Soc.* **2014**, *161*, F734.
[5] A. Hagen, G. B. Johnson, P. Hjalmarsson, *J. Power Sources* **2014**, *272*, 776.
[6] A. Weber, S. Dierickx, A. Kromp, E. Ivers-Tiffée, *Fuel Cells* **2013**, *13*, 487.
[7] M. Riegraf, V. Yurkiv, G. Schiller, R. Costa, A. Latz, K. A. Friedrich, *J. Electrochem. Soc.* **2015**, *162*, F1324.

[8] S. Kavurucu Schubert, M. Kusnezoff, A. Michaelis, S. I. Bredikhin, *J. Power Sources* **2012**, *217*, 364.

[9] J. P. Trembly, A. I. Marquez, T. R. Ohrn, D. J. Bayless, *J. Power Sources* **2006**, *158*, 263.

[10] J. P. Ouweltjes, P. V. Aravind, N. Woudstra, G. Rietveld, *J. Fuel Cell Sci. Technol.* **2006**, *3*, 495.

[11] P. V. Aravind, J. P. Ouweltjes, N. Woudstra, G. Rietveld, *Electrochem. Solid-State Lett.* **2008**, *11*, B24.

[12] C. Xu, P. Gansor, J. W. Zondlo, K. Sabolsky, E. M. Sabolsky, *J. Electrochem. Soc.* **2011**, *158*, B1405.

[13] L. Zhang, S. P. Jiang, H. Q. He, X. Chen, J. Ma, X. C. Song, *Int. J. Hydrogen Energy* **2010**, *35*, 12359.

[14] E. Brightman, D. G. Ivey, D. J. L. Brett, N. P. Brandon, *J. Power Sources* **2011**, *196*, 7182.

[15] P. Lohsoontorn, D. J. L. Brett, N. P. Brandon, *J. Power Sources* **2008**, *183*, 232.

[16] C. Zhang, M. E. Grass, A. H. McDaniel, S. C. DeCaluwe, F. El Gabaly, Z. Liu, K. F. McCarty, R. L. Farrow, M. A. Linne, Z. Hussain, G. S. Jackson, H. Bluhm, B. W. Eichhorn, *Nat. Mater.* **2010**, *9*, 944.

[17] W. C. Chueh, Y. Hao, W. Jung, S. M. Haile, *Nat. Mater.* **2012**, *11*, 155.

[18] W. C. Chueh, S. M. Haile, *Phys. Chem. Chem. Phys.* **2009**, *11*, 8144.

[19] Z. A. Feng, F. El Gabaly, X. Ye, Z.-X. Shen, W. C. Chueh, *Nat. Commun.* **2014**, *5*, 1.

[20] S. C. Decaluwe, M. E. Grass, C. Zhang, F. El Gabaly, H. Bluhm, Z. Liu, G. S. Jackson, A. H. McDaniel, K. F. McCarty, R. L. Farrow, M. A. Linne, Z. Hussain, B. W. Eichhorn, *J. Phys. Chem. C* **2010**, *114*, 19853.

[21] T. Nakamura, T. Kobayashi, K. Yashiro, A. Kaimai, T. Otake, K. Sato, J. Mizusaki, T. Kawada, *J. Electrochem. Soc.* **2008**, *155*, B563.

[22] B. Iwanschitz, J. Sfeir, A. Mai, M. Schütze, *J. Electrochem. Soc.* **2010**, *157*, B269.

[23] V. Papaefthimiou, M. Shishkin, D. K. Niakolas, M. Athanasiou, Y. T. Law, R. Arrigo, D. Teschner, M. Hävecker, A. Knop-Gericke, R. Schlögl, T. Ziegler, S. G. Neophytides, S. Zafeiratos, *Adv. Energy Mater.* **2013**, *3*, 762.

[24] S. Primdahl, M. Mogensen, *Solid State Ionics* **2002**, *152*, 597.

[25] S. Primdahl, Y. L. Liu, *J. Electrochem. Soc.* **2002**, *149*, A1466.

[26] M. Chen, B. H. Kim, Q. Xu, B. G. Ahn, D. P. Huang, *Solid State Ionics* **2010**, *181*, 1119.

[27] P. Kim, D. J. L. Brett, N. P. Brandon, *J. Power Sources* **2009**, *189*, 1060.

[28] W. C. Chueh, S. M. Haile, *Annu. Rev. Chem. Biomol. Eng.* **2012**, *3*, 313.

[29] J. Fleig, *Phys. Chem. Chem. Phys.* **2005**, *7*, 2027.

[30] V. Yurkiv, R. Costa, Z. Ilhan, A. Ansar, W. G. Bessler, *J. Electrochem. Soc.* **2014**, *161*, F480.

[31] H. Kishimoto, K. Yamaji, T. Horita, Y.-P. Xiong, *Electrochemistry* **2009**, *77*, 190.

[32] H. He, R. J. Gorte, J. M. Vohs, *Electrochem. Solid-State Lett.* **2005**, *8*, A279.

[33] P. Lohsoontorn, D. J. L. Brett, N. P. Brandon, *J. Power Sources* **2008**, *175*, 60.

[34] B. Mirfakhraei, S. Paulson, V. Thangadurai, V. Birss, *J. Power Sources* **2013**, *243*, 95.

[35] D. R. Mullins, T. S. McDonald, *Surf. Sci.* **2007**, *601*, 4931.

[36] W. G. Bessler, S. Gewies, *J. Electrochem. Soc.* **2007**, *154*, B548.

[37] S. Primdahl, *J. Electrochem. Soc.* **1999**, *146*, 2827.

[38] S. Gewies, W. G. Bessler, *J. Electrochem. Soc.* **2008**, *155*, B937.

[39] A. Babaei, S. P. Jiang, J. Li, *J. Electrochem. Soc.* **2009**, *156*, B1022.

[40] R. Barfod, M. Mogensen, T. Klemensø, A. Hagen, Y.-L. Liu, P. Vang Hendriksen, *J. Electrochem. Soc.* **2007**, *154*, B371.

[41] M. Kornely, A. Neumann, N. H. Menzler, A. Leonide, A. Weber, E. Ivers-Tiffée, *J. Power Sources* **2011**, *196*, 7203.

[42] Y. Tao, S. D. Ebbesen, M. B. Mogensen, *J. Electrochem. Soc.* **2014**, *161*, F337.

[43] M. Vogler, A. Bieberle-Hütter, L. Gauckler, J. Warnatz, W. G. Bessler, *J. Electrochem. Soc.* **2009**, *156*, B663.

[44] L. Jia, X. Wang, B. Hua, W. Li, B. Chi, J. Pu, S. Yuan, L. Jian, *Int. J. Hydrogen Energy* **2012**, *37*, 11941–11945.

[45] W. An, D. Gatewood, B. Dunlap, C. H. Turner, *J. Power Sources* **2011**, *196*, 4724–4728.

[46] A. Hagen, *J. Electrochem. Soc.* **2013**, *160*, F111.

[47] W. C. Chueh, W. Lai, S. M. Haile, *Solid State Ionics* **2008**, *179*, 1036.

[48] S. B. Adler, J. A. Lane, B. C. H. Steele, *J. Electrochem. Soc.* **1996**, *143*, 3554.

[49] C. Graves, C. Chatzichristodoulou, M. B. Mogensen, *Faraday Discuss.* **2015**, *182*, 75.

[50] Z. Cheng, S. Zha, M. Liu, *J. Power Sources* **2007**, *172*, 688.

[51] Z. Cheng, J.-H. Wang, Y. Choi, L. Yang, M. C. Lin, M. Liu, *Energy Environ. Sci.* **2011**, *4*, 4380.

[52] J. F. B. Rasmussen, A. Hagen, *J. Power Sources* **2009**, *191*, 534.

[53] K. Sasaki, K. Susuki, A. Iyoshi, M. Uchimura, N. Imamura, H. Kusaba, Y. Teraoka, H. Fuchino, K. Tsujimoto, Y. Uchida, N. Jingo, *J. Electrochem. Soc.* **2006**, *153*, A2023.

[54] I. Alstrup, J. Rostrup-Nielsen, S. Røen, *Appl. Catal.* **1981**, *1*, 303.

[55] D.-H. Lim, H. S. Kim, S. P. Yoon, J. Han, C. W. Yoon, S. H. Choi, S. W. Nam, H. C. Ham, *Phys. Chem. Chem. Phys.* **2014**, *16*, 10727.

[56] Y. Matsuzaki, I. Yasuda, *Solid State Ionics* **2000**, *132*, 261.

[57] A. Leonide, V. Sonn, A. Weber, E. Ivers-Tiffée, *J. Electrochem. Soc.* **2008**, *155*, B36.

[58] M. G. H. M. Hendriks, J. E. Ten Elshof, H. J. M. Bouwmeester, H. Verweij, *Solid State Ionics* **2002**, *146*, 211.

[59] W. C. Chueh, A. H. McDaniel, M. E. Grass, Y. Hao, N. Jabeen, Z. Liu, S. M. Haile, K. F. McCarty, H. Bluhm, F. El Gabaly, *Chem. Mater.* **2012**, *24*, 1876.

[60] M. Mogensen, T. Lindegaard, U. R. Hansen, G. Mogensen, *J. Electrochem. Soc.* **1994**, *141*, 2122.

[61] Z. Li, T. Mori, G. J. Auchterlonie, J. Zou, J. Drennan, Z. Li, T. Mori, G. J. Auchterlonie, J. Zou, *App. Phys. Lett.* **2014**, *093104*, 13.

[62] J. Fleig, *J. Power Sources* **2002**, *105*, 228.

[63] M. Gerstl, A. Nenning, R. Iskandar, V. Rojek-Wöckner, M. Bram, H. Hutter, A. Opitz, *Materials* **2016**, *9*, 649.

[64] D. Marrocchelli, B. Yildiz, *J. Phys. Chem. A* **2011**, *2*, 2411.

[65] E. Aneggi, J. Llorca, M. Boaro, A. Trovarelli, *J. Catal.* **2005**, *234*, 88.

[66] C. Lu, W. L. Worrell, J. M. Vohs, R. J. Gorte, *J. Electrochem. Soc.* **2003**, *150*, A1357.

[67] M. Miyake, S. Matsumoto, M. Iwami, S. Nishimoto, Y. Kameshima, *Int. J. Hydrogen Energy* **2016**, *1*, 2–8.

[68] S. Risse, N. A. Cañas, N. Wagner, E. Härk, M. Ballauff, K. A. Friedrich, *J. Power Sources* **2016**, *323*, 107.